Structures and effects of radiation damage in cuprate superconductors irradiated with several-hundred-MeV heavy ions

Yimei Zhu, Z. X. Cai, R. C. Budhani, M. Suenaga, and D. O. Welch
Materials Science Division, Department of Applied Science, Brookhaven National Laboratory, Upton, New York 11973
(Received 1 April 1993)

This paper reports a study of the nature and systematic variation of radiation damage to cuprate superconductors caused by several-hundred-MeV heavy ions. While irradiation of $YBa_2Cu_3O_{7-\delta}$ with 300-MeV Au^{24+} and 276-MeV Ag^{21+} ions produces columns of amorphous material along the ion trajectories, such defects are only created occasionally during irradiation with 236-MeV Cu^{18+} and not induced with 182-MeV Si^{13+}. A comparative study of the defect formation in $Bi_2Sr_2Ca_2Cu_3O_x$ and oxygen-reduced and ozone-treated $YBa_2Cu_3O_{7-\delta}$, shows that the degree of the radiation damage by the heavy ions depends on (a) the rate at which ions lose their energy in the target; (b) the crystallographic orientations with respect to the incident ion beam; (c) thermal conductivity and chemical state (oxygen concentration for $YBa_2Cu_3O_{7-\delta}$) of the sample; and (d) the extent of preexisting defects in the crystal. A theoretical model based on ion-induced localized melting and the effects of anisotropic thermal conductivity of these materials provides a basis for understanding the size and shape of the amorphous tracks. Measurements of the superconducting properties of Au^{24+}- and Ag^{21+}-irradiated $YBa_2Cu_3O_{7-\delta}$ thin films show a universal linear scaling between the fractional areal damage versus the superconducting transition temperature and the normal-state resistivity.

I. INTRODUCTION

Obtaining a high critical current density J_c requires strong pinning of flux lines in superconducting materials. To provide such pinning sites for the magnetic flux, defects have been deliberately and selectively created by irradiation with energetic electrons, γ rays, and nucleon (protons and neutrons) and α particles since the early days of type-II superconductors.[1] Recently, several groups have investigated the influence of radiation-induced point defects and small defect aggregates on the J_c of bulk ceramics, single crystals, and thin films of high-T_c cuprates.[2-5] However, the effectiveness of such defects in pinning the flux lines in a temperature range where thermal fluctuations are important has been disappointing. Intuitively, the short coherence length ξ and large fluctuation effects in high-T_c cuprates suggest that linear defects which pin along the entire length of a flux line might be more effective. Indeed, the linear tracks of amorphized material created by heavy ions of several-hundred-MeV energy have been found to provide strong flux pinning in the temperature and field regime where the effects of point defects are inconsequential.[6-13] In order to help elucidate the relationships between superconducting properties and the defects produced by heavy-ion irradiation, we have undertaken a systematic study of the defects in thin films and bulk samples of $YBa_2Cu_3O_{7-\delta}$ and $Bi_2Sr_2Ca_2Cu_3O_x$ created by irradiation with Au^{24+} (300-MeV), Ag^{21+} (276-MeV), Cu^{18+} (236-MeV), and Si^{13+} (182-MeV) ions. A preliminary account of this study can be found in Ref. 15. As described in detail below the structure of the defects was characterized by transmission-electron microscopy (TEM) and high-resolution electron microscopy (HREM), combined with nanoprobe chemical analyses using energy-dispersive x-ray spectroscopy (EDX) and electron-energy-loss spectroscopy (EELS). These studies clearly show that the radiation-induced defects consist of severe chemical and structural local disorder. The degree of damage caused by the ions varies with the ion energy-deposition rate and species of ion, varying from Au, Ag, Cu, to Si in the order of decreasing severity. Furthermore, for all these ions, the density and size of the defects depend strongly on oxygenation of the sample, orientation of the crystal with respect to the ion beam, as well as on the presence of previously existing imperfections in the lattice. These changes can be attributed largely to differences of the thermal conductivity of the materials and a thermal spike model was developed to provide a theoretical framework for the discussion of the variation of size and shape of the amorphous tracks under various conditions. The investigation of the effects of the heavy-ion-induced defects on flux pinning and critical current density have been reported elsewhere.[12,13] However, we report here the systematic variation of their effect on the normal-state resistivity and critical temperature T_c since this has some bearing on the damage to the matrix outside the area of the defects which is imaged by TEM.

II. EXPERIMENTAL METHODS

A. Sample preparation

Both thin films and bulk samples were used for the present studies. Thin films of $YBa_2Cu_3O_7$ were deposited *in situ* on (100)-cut $SrTiO_3$ plates by an off-axis magnetron sputtering technique. Standard sintering methods were employed to produce polycrystalline $YBa_2Cu_3O_{7-\delta}$ (Ref. 14) while a high-temperature pressing technique

was used to produce c-axis aligned textured $Bi_2Sr_2Ca_2Cu_3O_x$ bulk samples.[15] Oxygen-deficient samples ($YBa_2Cu_3O_{6.3}$) were prepared by quenching the sintered samples from 950 °C into liquid nitrogen.

TEM specimens were made by slicing the sintered pellets, ultrasonically cutting out 3-mm disks, mechanically dimpling them to ~ 10 μm thick, and finally ion-milling them at 3–4 keV at a 8°–10° tilt angle with a Gatan low-energy gun. Most of the $YBa_2Cu_3O_{7-\delta}$ TEM samples were stored in a desiccator for more than six months before they were used. However, in all cases, the samples were cleaned and examined before irradiation. Their oxygen substoichiometry δ was estimated as $\delta < 0.1$. Some samples were subjected to ozone oxygenation at 200 °C for 2–5 h.[16] Flowing ozone gas was produced by an ozone generator, consisting of ultraviolet radiation from a low-pressure mercury lamp in the presence of 1 atm pressure of oxygen. These prethinned bulk samples and thin films were subsequently irradiated with heavy ions.

B. Heavy-ion irradiation

Thin crystals, either thin films and ion-thinned TEM samples, were irradiated by various heavy ions at room temperature. Ions of Au^{24+}, Ag^{21+}, Cu^{18+}, and Si^{13+} were produced in a Tandem Van de Graaff accelerator at Brookhaven National Laboratory. The ion beam was incident at 5° off the sample normal to avoid possible channeling. In Table I we list the flux (as measured with an annular Faraday cup), the energy, the charge state, and the range (mean penetration depth) of these ions for $YBa_2Cu_3O_{7-\delta}$ and $Bi_2Sr_2Ca_2Cu_3O_x$. Since the thickness of the samples used here is negligibly small compared to the range of these ions, the linear energy transfer (LET) of the projectiles in the stopping medium can be regarded as constant. This ensures uniform damage tracks along the thickness of the samples.

C. Electron microscopy and electron-energy-loss spectroscopy (EELS)

The microstructure of all samples before and after irradiation was examined with transmission electron microscopes (JEOL 2000FX and JEOL 2010) operated at 200 keV, using phase- and diffraction-contrast imaging. Oxygen concentration was analyzed by EELS, monitoring the oxygen K-edge prepeak (~ 528 eV). EELS spectra were acquired using a JEOL 2000FX (LaB_6 source) and a Phillips 400T (field-emission source) electron microscope equipped with a liquid-nitrogen holder. A Gatan 666 PEELS spectrometer with an attached multichannel analyzing system was used to collect the EELS spectrum. The energy resolution of the spectrometer, as determined by the full width half maximum (FWHM) of the zero-loss peak, was better than 0.7 eV for an undersaturated electron beam, but was about 1.5–2 eV under most experimental conditions. Acquisition time was limited to 6 s to minimize the possible drift of specimen (mechanical) and spectrum (electronic), and possible beam damage of the area during the acquisition period. The technical aspects of the EELS experiments have been described elsewhere.[17]

D. Measurements of superconducting properties

The effects of the heavy-ion damage on the normal-state resistivity and the critical temperature of thin films of $YBa_2Cu_3O_{7-\delta}$ were measured. The thin films were photolithographically patterned in the form of 1-mm-long and 100-μm-wide bridges for a four-probe measurement of resistivity and J_c. Low-resistivity contacts were achieved by depositing 200-nm silver pads onto which the current and voltage leads were attached with indium solder. Resistivity was measured with a 11.6 Hz excitation current of magnitude low enough to ensure a linear response and the voltage was measured with a lock-in amplifier. Current-voltage (I-V) characteristics were measured with a pulsed dc technique. The maximum transport current used in the I-V measurements was limited to 100 mA.

III. STRUCTURE OF THE DEFECTS INDUCED BY HEAVY-ION IRRADIATION

A. General morphology of the induced structural defects

Figure 1 shows typical morphology of a $YBa_2Cu_3O_{7-\delta}$ bulk sample irradiated with 300 MeV gold ions. Diffraction-contrast imaging reveals the presence of massive disks induced by irradiation when the crystals were viewed along the direction of incident ion beam [Fig. 1(a)]. Small variations in sharpness at the edge of the disk images suggests that some of the ion projectiles were

TABLE I. The energy, charge state, and fluence of various ions used in the present study and the estimated linear energy transfer and mean penetration depth, calculated using the tables of Ziegler (Ref. 30) for $YBa_2Cu_3O_{7-\delta}$ and $Bi_2Sr_2Ca_2Cu_3O_x$ (denoted by the asterisk).

Ion	Au	Ag	Cu	Si
Energy (MeV)	300	276	236	182
Charge	24	21	18	13
Fluence (ions/cm^2/s)	5.6×10^{10}	5.0×10^{10}	4.0×10^{11}	6.6×10^{10}
Energy loss (keV/nm)	34.8	23.8	13.4	3.8
	31.5*	21.8*	12.4*	2.5*
Range (μm)	14.1	15.7	19.2	37.5
	15.9*	17.7*	21.6*	42.0*

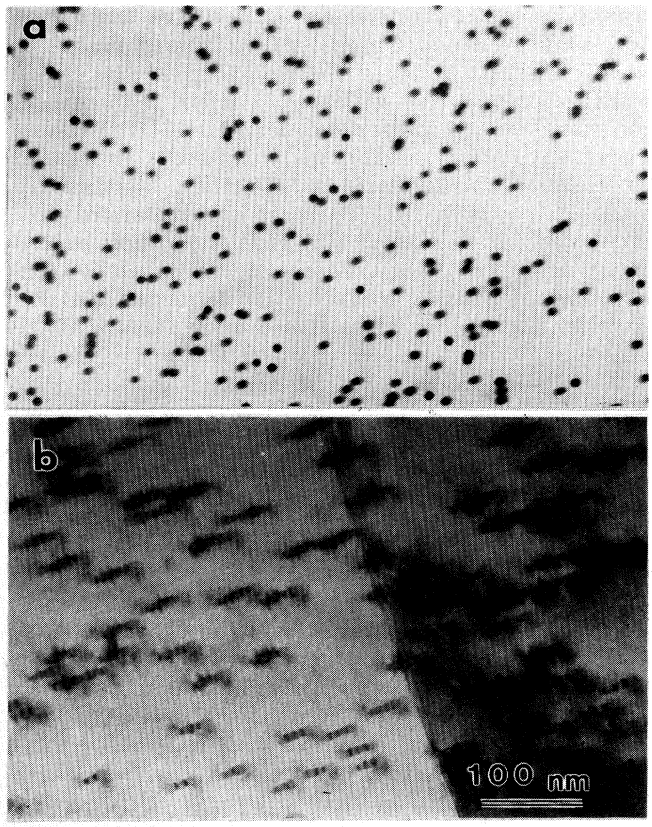

FIG. 1. Typical morphology of the Au^{24+}-radiation-induced defects viewed (a) along the ion track, (b) about 18° away from the ion track.

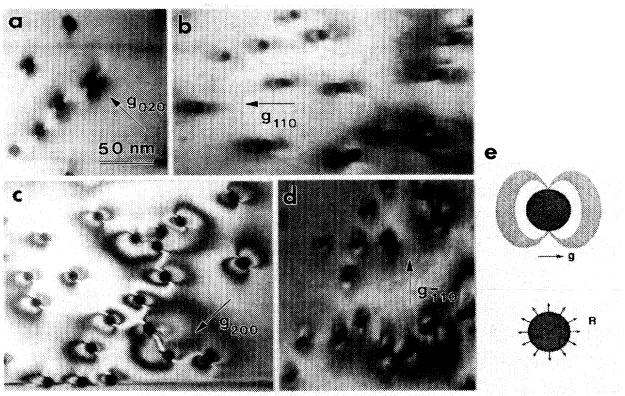

FIG. 2. Strain contrast surrounding the columnar defects imaged using diffraction vectors (a) $\mathbf{g}=020$, (b) $\mathbf{g}=110$, (c) $\mathbf{g}=200$, and (d) $\mathbf{g}=-110$. Note the contrast disappears in the direction perpendicular to the $\mathbf{g}$. (e) Sketches of the strain contrast and the displacement field due to the columnar defect.

weakly scattered after they entered the crystal. When the crystals were viewed away from the incident ion beam, the disks appear as rods, a clear indication that the defects are ion trajectories or ion tracks [Fig. 1(b)]. The rods, running from the top to the bottom of the sample, give rise to thickness fringes as well as to contrast due to its intersection with the specimen surface and crystal matrix. Nanodiffraction from the damaged regions with a probe size less than 2 nm (smaller than the diameter of the defect) shows that they are amorphous. By tilting the specimen through 60° and observing the same defects, we conclude that the ion-induced defects are continuous columns with severe lattice distortion throughout the thickness of the specimen.

Careful observations show that, under two-beam conditions, these defects also generate dark images consisting of lobes of contrast over an area two to three times larger than the diameter of the ion track. We characterized the contrast surrounding the defects using the weak-beam technique under different diffraction conditions. Figure 2 shows the black contrast associated with the columnar defects imaged by using diffraction vectors $\mathbf{g}=020$ [Fig. 2(a)], $\mathbf{g}=110$ [Fig. 2(b)], $\mathbf{g}=200$ [Fig. 2(c)], and $\mathbf{g}=-110$ [Fig. 2(d)] near the [001] axis (parallel to the incident ions). We found that the lobe contrast disappears only along the line perpendicular to the diffraction vector, $\mathbf{g}$, and running across the center of the damaged area. The main features of the contrast are similar to those observed for spherical precipitates in alloys,[18] but it has a different shape and is much smaller. We attribute the lobe contrast to radial strain/displacement fields surrounding the amorphous columnar defect [Fig. 2(e)]. The strain and structural disorder of the amorphous region propagates into the crystal lattice in a direction perpendicular to the ion track.

The strain contrast around the ion tracks can be modeled quantitatively[19] by treating the amorphous region as a misfitting elastic cylinder in an elastic matrix and calculating the contrast by the method of Ashby and Brown.[20] For an isolated amorphous track in an infinite matrix parallel to the c axis, with the assumption that the matrix is approximately elastically isotropic in the a-b plane and neglecting the difference in elastic constants between the amorphous and crystalline regions, linear elasticity theory[21] yields a radially symmetric displacement field $u(r)$ in the matrix around the ion track given by

$$u(r)=E_{\text{eff}}(R^2/r)\ , \tag{1}$$

where R is the radius of the amorphous track and

$$E_{\text{eff}}\equiv[(C_{11}+C_{12})E_{ab}+C_{13}E_c]/2C_{11}\ ,$$

where the C_{ij} are elastic constants and E_{ab} and E_c are the fractional strains upon amorphization along the a (or b) and c directions, respectively. Detailed comparison between the calculated and observed contrast for $YBa_2Cu_3O_7$ crystals yields $E_{\text{eff}}\cong 0.02$.[19]

B. Comparisons of the radiation damage created by Au, Ag, Cu, and Si ions

In order to investigate the influence of the atomic number of the irradiating ion on the radiation damage, we studied the structural defects induced in bulk $YBa_2Cu_3O_{7-\delta}$ by Au, Ag, Cu, and Si ions, with energies

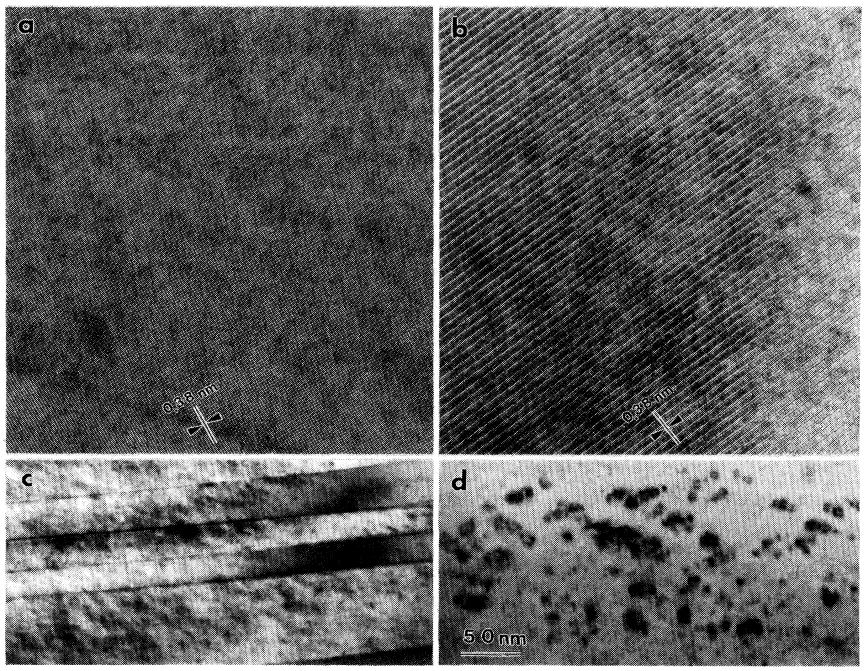

FIG. 3. TEM micrographs on Si-irradiated samples: (a) lattice images of a [001] projection, (b) [100] projection, (c) low-magnification two-beam image, and (d) dislocation loops.

and energy deposition rates listed in Table I. For Au and Ag ions, the irradiation yields a large number of columnar defects that are distributed randomly throughout the sample (Fig. 1). Nevertheless, each ion does not necessarily give rise to a single amorphous column. We found that the density of the defects strongly depends on the ion type and its energy, and the chemical state of the target material.

Si has the smallest atomic number of the four ions used. For Si-ion irradiation at 182 MeV, no columnar defect was observed in any samples which we examined, at least for a fluence of 6.6×10^{10} ions/cm^2. Figures 3(a) and 3(b) show HREM images of the [001] and [010] projections, respectively, from Si-irradiated $YBa_2Cu_3O_{7-\delta}$ ($\delta<0.1$). No distinct structural damage running through the sample thickness was seen. Occasionally, we observed weak strain contrast at and near the specimen surface [Fig. 3(c)], and a high density of dislocation loops, with diameters ranging from 10 to 20 nm [Fig. 3(d)]. Similar observations were made in samples irradiated by neutrons[22] and protons.[23] However, it is still not clear whether these defect features can be attributed to the irradiation, because such defects can sometimes be seen in as-grown $YBa_2Cu_3O_{7-\delta}$.

For Cu irradiation at 236 MeV, amorphous tracks were only occasionally observed for $YBa_2Cu_3O_{7-\delta}$ ($\delta<0.1$) when the ion beam was directed along the *a* (or *b*) direction. The concentration of the damaged regions varied between samples and also between areas of the same sample. Figures 4(a) and 4(b) show two areas from the same sample viewed near the [001] axis of $YBa_2Cu_3O_{7-\delta}$ ($\delta<0.1$). The structural damage is more severe in Fig. 4(b), where the black dots seen are strain contrast; however, no amorphous columns were seen by HREM in either area. Columnar defects were occasionally observed only when the ion beam was directed along the *a* (or *b*) axis.

Since, as discussed above, the observed columnar defect density due to the copper and silicon ions was small and variable in nature, the relation between the ion dose and the number of defects per unit area was assessed only for Au and Ag ions (Fig. 5). The density of the defects was measured over 100 areas of a fixed size (~0.2 μm^2)

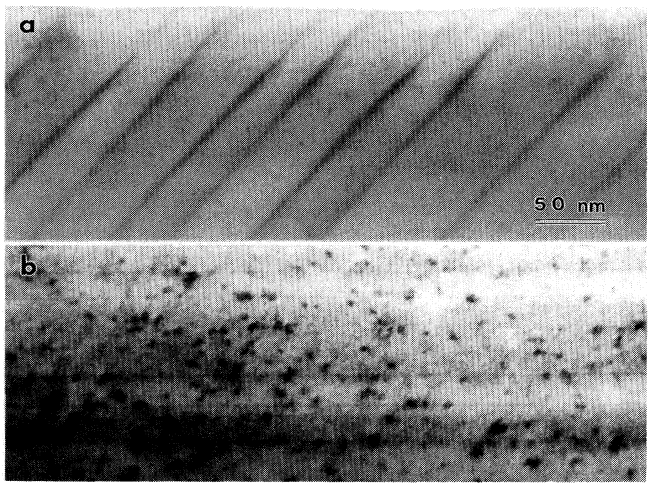

FIG. 4. The degree of the radiation damage seen in TEM caused by Cu ions varies with location in the specimen. (a) and (b) are views with the electron beam near the [001] axis of two different regions of a sample of $YBa_2Cu_3O_{7-\delta}$ ($0.1<\delta<0$). Note, the defects do not exhibit the same type of strain contrast shown by "regular" columns, as in Fig. 2. In some areas, even the weak strain contrast seen in (b) cannot be observed. [The approximately linear features seen in (a) and (b) are twin boundaries.]

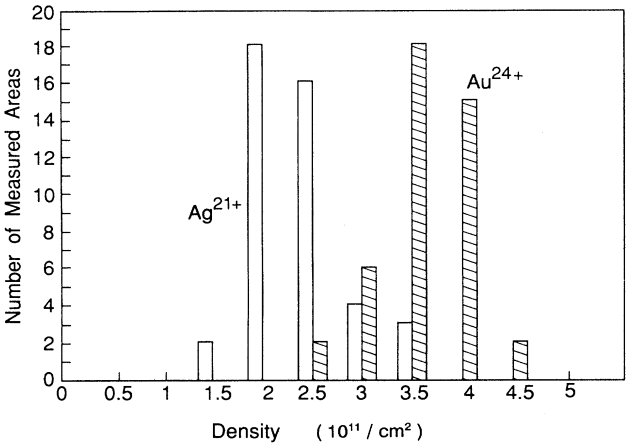

FIG. 5. A comparison of the columnar defect densities observed by TEM in ~100 areas of fixed size (~0.2 μm^2) for Au- and Ag-irradiated samples of $YBa_2Cu_3O_{7-\delta}$ ($\delta < 0.1$).

from TEM micrographs. For Au-ion radiation, the dose was 3.86×10^{10} ions/cm^2, a value that is very close to the average density we measured (3.7×10^{10} ions/cm^2). Thus, each Au ion produces a single columnar defect. However, for the Ag-ion irradiation, the measured density of the defects was about 2.5×10^{10} ions/cm^2, only half of the original dose of 5×10^{10} ions/cm^2. It appears that many Ag ions do not produce columnar defects during the irradiation process. The probability of forming columnar defects with Ag is thus smaller than for Au.

The size of the columnar defects also depends on the atomic number and energy of the ions used for irradiation. We examined more than one thousand [100] (or [010]) ion tracks produced by Au, Ag, and Cu irradiation. Their size was measured on HREM micrographs of lattice images surrounding the amorphous columns from regions less than 15 nm thick. Since the columnar defects have a well-defined facet along the *a-b* plane, counting the number of *a-b* planes lost in the amorphous region gives measurements of very high accuracy (less than a *c*-lattice constant, i.e., 1.179 nm). Figure 6 shows the size (diameter of the amorphous column in units of the *c*-lattice parameter) distribution of the defects produced by Au, Ag, and Cu ions in $YBa_2Cu_3O_{7-\delta}$ ($\delta < 0.1$). The dominant diameter of the defects was 10.6 nm (nine units of *c* lattice) for Au-irradiated samples, while 5.9 nm (five units of *c* lattice) for Ag-irradiated samples, and 2.36 nm (two units of *c* lattice) for Cu-irradiated samples. This finding clearly shows that irradiation with 300-MeV Au ions causes more severe lattice damage compared with 276-MeV Ag and 236-MeV Cu ions. It is interesting to note that while the size distribution of Au- and Ag-produced defects show a more-or-less Gaussian distribution, the Cu-induced defects follow an approximate half-Gaussian distribution since those defects with a size less than a *c*-lattice parameter were not counted.

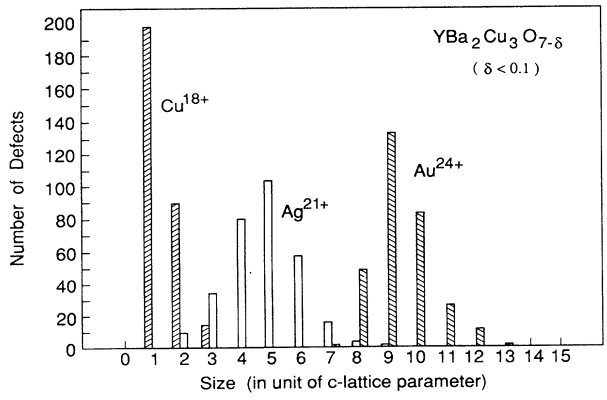

FIG. 6. Size distribution of the defects induced by Au, Ag, and Cu in nominal $YBa_2Cu_3O_{7-\delta}$ ($0.1 < \delta < 0$). The dominant size of the defects was 10.6 nm (nine units of *c* lattice) in diameter for Au-radiated samples, 5.9 nm (five units of *c* lattice) for Ag-radiated samples, and 2.36 nm (two units of *c* lattice) for Cu-irradiated samples.

C. Dependence of the radiation damage on the crystallographic orientations of the incident ions

At low magnification, as shown in Fig. 1, the defects appear to have a circular symmetry along the ion trajectory in all orientations. However, HREM shows that the morphology of the defects depends on the direction of the incident ions with respect to the crystallographic axes of the material. Figures 7(a) and 7(b) show high-resolution images of the Au^{24+} irradiation-induced defects in bulk $Bi_2Sr_2Ca_2Cu_3O_x$ viewed along the [100] and the [001] direction, respectively. The amorphism of the damaged area is clearly visible. When the ion track is parallel to the *c* axis [Fig. 7(b)], the defects appear as circular disks (~16 nm in diameter). In contrast, when the ion track is parallel to the *a* or *b* axis [Fig. 7(a)], the defects appear somewhat larger and elliptical, with a size about 18 nm×21 nm. In the latter case, the edge of the amorphous region shows well-defined facets in the *a-b* planes and, near the short axis of the ellipse, always terminates sharply at the *a-b* planes, or more precisely, between the BiO double layers. At the periphery near the long axis of the ellipse, the interface between the defect and the crystal matrix is diffuse (extending about two unit cells) and is similar to the interface observed [Fig. 7(a)] when the defect is formed by an ion beam parallel to the *c* axis.

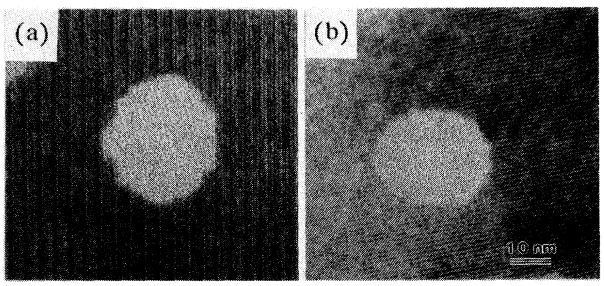

FIG. 7. High-resolution images of Au^{24+} irradiation-induced defects in bulk $Bi_2Sr_2Ca_2Cu_3O_x$ recorded in (a) [100], and (b) [001] projections, respectively.

The variation of the high-resolution images of the defects in $YBa_2Cu_3O_{7-\delta}$ with respect to the crystallographic orientation was essentially identical to that seen in $Bi_2Sr_2Ca_2Cu_3O_x$, i.e., circular cross sections for ions incident along [001] direction, and elliptical for those along the [100] or [010] direction. However, the size of the defects was smaller by a factor of 0.5–0.7 than those in $Bi_2Sr_2Ca_2Cu_3O_x$. The orientational dependence of the shape of the defect was very clearly illustrated for an irradiated $YBa_2Cu_3O_{7-\delta}$ ($\delta \approx 0.0$) thin film containing a mixture of grains with *a* and *c* orientations (Fig. 8), where the areas denoted *A* and *C* have the *a* (or *b*) and *c* axes parallel to the film normal, respectively. The difference in morphology of the defects between [001] and [100] (or [010]) orientations is clear. We conclude that an ion beam directed along the *a* or *b* axis causes more severe structural damage than a beam along the *c* axis. The interpretation of this observation is addressed in Sec. V.

D. Dependence of the radiation damage on oxygen concentration in $YBa_2Cu_3O_{7-\delta}$

We observed that the extent of radiation damage depends on the oxygen stoichiometry of the sample. To elucidate this dependence, we irradiated oxygen-deficient and fully oxygenated samples. Differences between Ag-irradiation-induced defects in $YBa_2Cu_3O_{7-\delta}$ are shown in Fig. 9 for samples with (a) $\delta \approx 0.7$, (b) $\delta < 0.1$, and (c) $\delta \approx 0.0$ (ozone oxygenated). All the micrographs show lattice images viewed along the [100] axis. In Figs. 9(b) and 9(c), the direction of the incident beam was slightly off from the [100] projection and, therefore, only near the edge of the specimen (bottom part of the micrographs) the defects are end-on and appear as white contrast. The differences in the size and the density of the damage among the various samples are remarkable. For $YBa_2Cu_3O_{6.3}$, the average size of the defects is close to that observed in Au-irradiated $YBa_2Cu_3O_{7-\delta}$ ($\delta < 0.1$), while for $YBa_2Cu_3O_{7-\delta}$ ($\delta \approx 0.0$) the size is close to that observed in the Cu-irradiated material. The size distribution of the defects for these three samples is plotted in Fig. 10. The sizes were measured by counting the numbers of *a-b* planes across the area. The average diameter of the amorphous regions for $YBa_2Cu_3O_{6.3}$ was 7.8 nm, for $YBa_2Cu_3O_{7-\delta}$ ($\delta < 0.1$) it was 5.3 nm, and for $YBa_2Cu_3O_{7-\delta}$ ($\delta \approx 0.0$) it was 3.3 nm. It is important to note that a small decrease of the oxygen substoichiometry (δ from 0.1 to 0.0), significantly reduced the radiation damage.

As shown above (Fig. 4), the probability of formation of the columnar defects varies from area to area for Cu-irradiated $YBa_2Cu_3O_{7-\delta}$ ($\delta < 0.1$). This variability appears to be due to oxygen inhomogeneity in the as-prepared TEM specimen from a nominal fully oxygenated sample. In general, no columnar defect were observed except when the ion beam was directed along the *a-b*

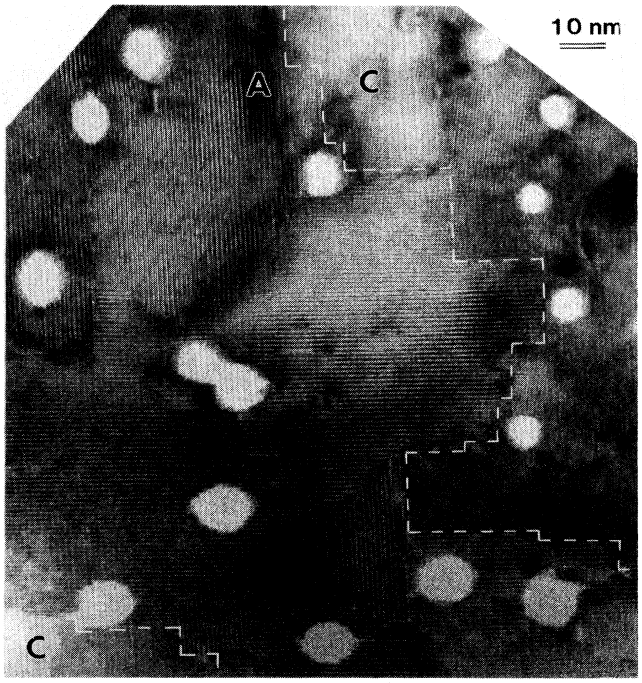

FIG. 8. High-resolution image of Au^{24+}-irradiated $YBa_2Cu_3O_7$ thin film. The defects appear elliptical in shape when the incident ion is parallel to the [100] (or [010]) direction, but smaller and circular in shape when parallel to the [001] direction. The areas denoted *A* and *C* have the *a* (or *b*) and *c* axes parallel to the film normal, respectively.

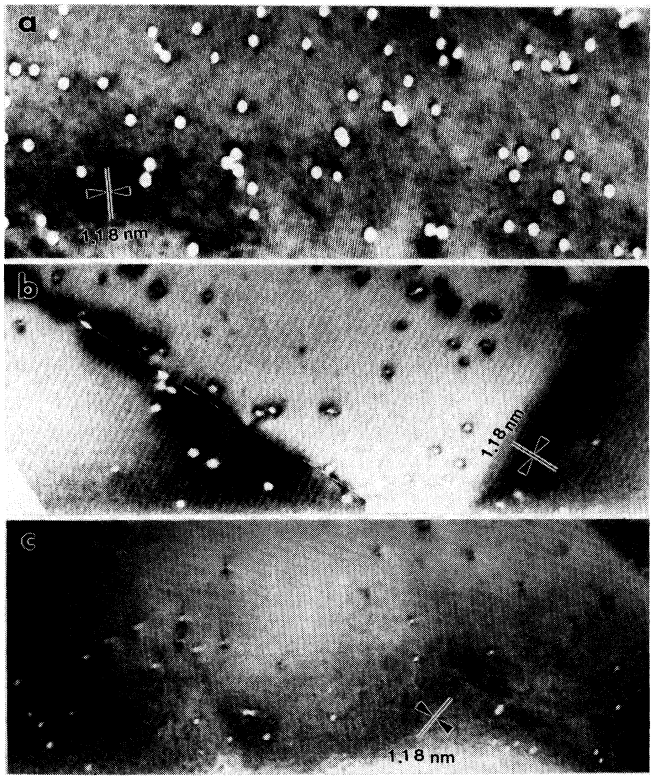

FIG. 9. Columnar defects induced by Ag-ion radiation viewed along [100] direction. (a) $YBa_2Cu_3O_{6.3}$, (b) $YBa_2Cu_3O_{7-\delta}$ ($0 < \delta < 0.1$), and (c) ozone-treated $YBa_2Cu_3O_{7-\delta}$ ($\delta \approx 0$).

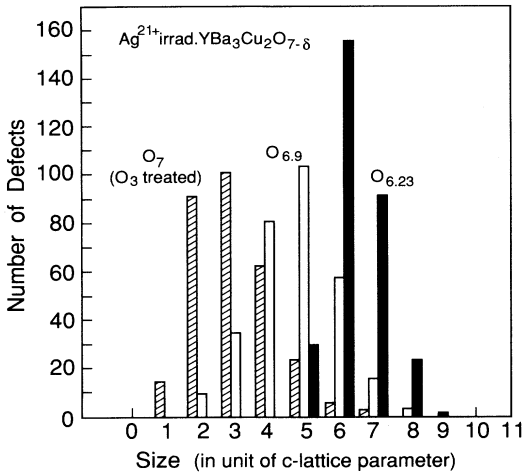

FIG. 10. Size distribution of Ag-radiation-induced defects for the three samples shown in Fig. 9.

plane. Defects which appear to consist of columns continuously amorphisized along the ion track are marked by arrows in Fig. 11(a). However, the majority of the defects exhibit a lattice-image across the damaged region,

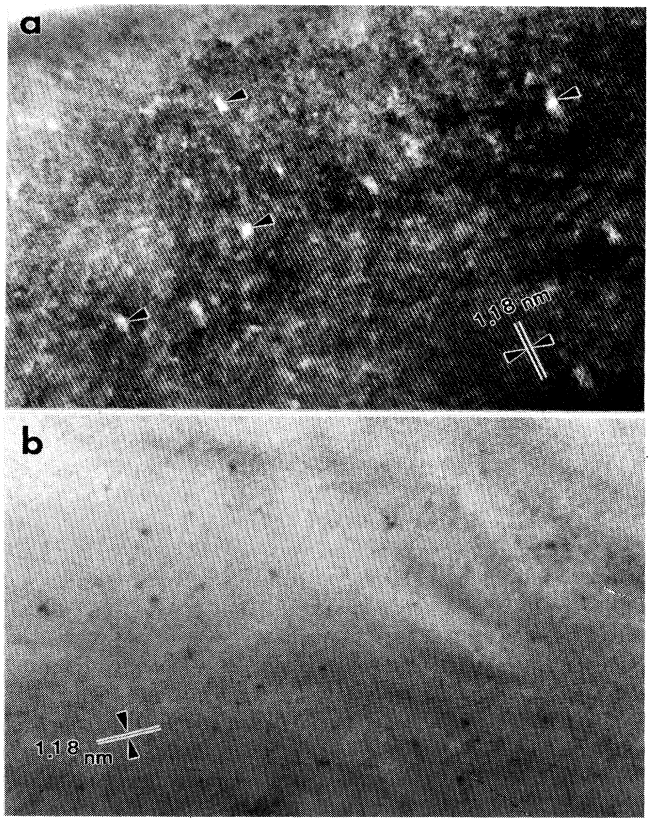

FIG. 11. Lattice image of [001] projection observed in $YBa_2Cu_3O_{7-\delta}$. (a) Cu ion irradiated without ozone treatment. The arrows denote defects in which the amorphous column extends completely through the sample. Other defects can be seen which show a superposition of amorphous and crystalline regions along the ion track. (b) Cu ion irradiated after ozone treatment.

presumably the supposition of an amorphous region and a crystal lattice, possibly because of an intermittent amorphization along the ion track. In contrast, in samples oxygenated with ozone, the damage induced by Cu irradiation was much less than that in oxygen-deficient samples. Even when the ion-beam is parallel to the (*a* or *b*) axis, only a low-density strain contrast (appearing as black dots) was visible [Fig. 11(b)]. This is consistent with the observations of the effects of Ag-ion irradiation and suggests that the radiation damage of $YBa_2Cu_3O_{7-\delta}$ depends strongly on the oxygen concentration.

E. Dependence of the radiation damage on the presence of crystal imperfections

We found that preexisting imperfections in the crystal also play an important role in forming the columnar defects. Such an effect is not clearly visible for Au irradiation because each Au ion always produces a single amorphous column, regardless of the target crystal. However, for a lighter and less energetic ion such as Cu, we demonstrated that the formation of the amorphous zone is very sensitive to the characteristics of the crystal, depending not only on the orientation of the crystal and oxygen concentration but also on the presence of imperfections in the crystal. Shown in Fig. 12 is an example of a (001) lattice image from an area with preexisting planar defects. In contrast with our observations of preexisting-defect-free areas of ozone-treated sample irradiated with Cu, which show no amorphous columnar defects regardless of the orientation, here we observed a high density of columnar defects with an average size ~ 2.2 nm. Furthermore, the distribution of these defects is not random. The radiation-induced defects seen in Fig. 12 are formed only at the location (marked as *B*) of stacking faults (appearing as white lines, viewed here edge-on). In the area marked *A*, there were no stacking faults, and no columnar defects were formed there. Such stacking faults, characterized as having a plane normal of [001] and a displacement vector of $\frac{1}{6}$ [301], were sometimes observed in the as-grown samples and ozone-annealed samples. From these results, we conclude that structural imperfections in the as-grown crystal enhance radiation damage, especially in the case of planar defects such as stacking faults or

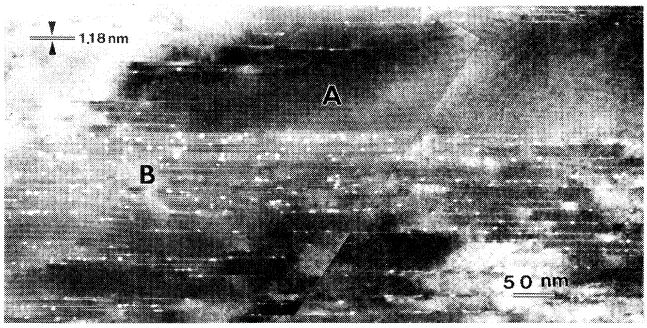

FIG. 12. (100) lattice image of an ozone-treated sample of $YBa_2Cu_3O_{7-\delta}$ ($\delta \cong 0$) irradiated with Cu ions. Note, the columnar defects were only observed at the location of the preexisting stacking faults.

grain boundaries when their plane normal is perpendicular to the incident ion beam.

F. Creation of stacking faults by heavy-ion damage

Planar defects associated with the amorphous columns are frequently observed in Au^{24+}- and Ag^{21+}-irradiated $YBa_2Cu_3O_{7-\delta}$ $(0.05<\delta<0.6)$. These planar defects were created by the damage, unlike those discussed in the previous section. They are clearly visible when the electron beam is parallel to the *a-b* plane (Fig. 13). The extension of the fault is about 3–5 times of the radius of the amorphous column. Similar defects, characterized as intrinsic and extrinsic stacking faults with a (001) plane normal, were observed in quenched $YBa_2Cu_3O_{7-\delta}$.

Detailed analysis of high-resolution images of the faults yielded a determination of its character. The displacement vector of the faults is either $\mathbf{R}=\frac{1}{6}[031]$ or $\mathbf{R}=\frac{1}{6}[032]$. Thus, the observed planar defect consists of two stacking faults bounded by a partial dislocation at each end. Since the motion of such a dislocation does not give rise to the observed fault, the formation of the fault must be chemical in nature. The above structure models are also consistent with the observation of the Cu enrichment in such planar defects induced by heavy-ion irradiation by a high-resolution EDX measurement using a 2-nm probe.[24]

FIG. 13. (100) lattice image of $YBa_2Cu_3O_{7-\delta}$ $(\delta<0.1)$ irradiated with Ag ions showing stacking faults, viewed edge on, created by the radiation damage. The stacking faults are seen as dark wide lines in thick region and white narrow lines in thin region.

G. EELS measurements across the columnar defects

To characterize the chemical disorder within and near the irradiation-induced defects, the composition across the amorphous region of Au-irradiated samples was analyzed using a nanoprobe TEM (2 nm) combined with EDX. There was no noticeable difference ($<3\%$) in the cation composition in both the amorphous regions and the surrounding crystalline matrix, either for an ion beam parallel to the *a* /*b* direction or to the *c* direction.[24] However, for anion oxygen, we observed with EELS a remarkable change across the damaged area in the fine structure of the oxygen *K*-edge absorption spectrum, more precisely, the prepeak of the *K* edge. The prepeak represents transition of electrons from O 1*s* states into unoccupied states. The integrated intensity of the prepeak is a direct measure of the hole density near the Fermi level, and is usually proportional to the oxygen content.[17] The integrated intensity can also be diminished by disorder in the CuO chains.

Figure 14 shows a series of EELS spectra acquired over a span of 60 nm across the amorphous region. The acquisition step is about 5 nm and the acquisition probe is 2 nm in diameter. To compare the strength of the prepeak at 528 eV, we have normalized the data with respect to the main-peak at 537 eV. The spectra can be divided into three groups, denoted as spectra *A*, *B*, and *C*. (They are symmetrically acquired at the positions with respect to the center of the defect as shown in Fig. 14.) Spectra *A*, taken from positions more than 20 nm away from the center of the amorphous region, show a prepeak at about 528 eV (the oxygen prepeak would be much pronounced if a larger probe and a longer acquisition time were used[16]), similar to that observed in a defect-free crystalline matrix. Spectra *B*, acquired 10–15 nm away from the center of the amorphous region (5–10 nm from its edge), show the oxygen *K* edge rising straight up toward the main peak without a prepeak. In the amorphous region (Spectra *C*), not only was the prepeak absent, but also the height of the oxygen main peak was drastically reduced (only 70% of that observed in the spectra *A* and *B* before normalization of the intensity). This suggests that there was a marked change in electronic structure and possibly a loss of oxygen atoms from the amorphous region. An important observation here is the existence of spectra *B*, where the drastic change in the oxygen preedge peak suggests a decrease in the number of holes in the crystal near the amorphous region. The reduction of the hole content outside the defect can be due to a reduction in oxygen concentration, or disorder in the crystal lattice, particularly the oxygen in the Cu-O chains or perhaps to elastic strain. A comparison of the prepeak of the spectra *B* with the observations of Nücker *et al.*[25] and Takahashi *et al.*[26] suggests that the oxygen deficiency required to match the data is about $\delta\approx0.7$. However, the depression of the hole concentration surrounding the amorphous region might also be attributed to the lattice distortion around the defects, as seen in Fig. 2. Furthermore, theoretical estimates suggest that to generate one oxygen hole, an undistorted oxygen-chain should be at least five unit cells long,[27] thus radiation-

induced oxygen disorder may also be playing a role. Independent of its origin, it is clear that the reduction of the hole content near the columnar defect enlarges the weak- or nonsuperconducting area to almost twice as large as that of the amorphous region.

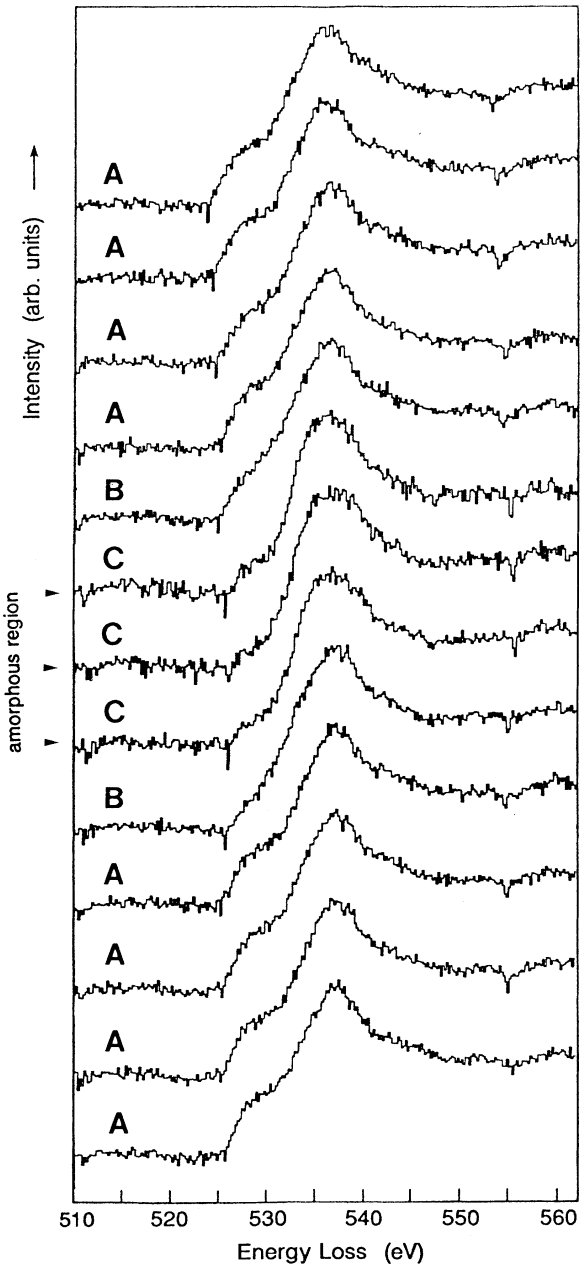

FIG. 14. A series of EELS spectra acquired over a span of 60 nm at and near the amorphous region. The acquisition step is about 5 nm, and the acquisition probe diameter is 2 nm. To compare the strength of the prepeak each spectrum was normalized by the oxygen main peak at 537 eV. Spectra labeled *A* and *B* were acquired from within the crystalline matrix around the defect while those labeled *C* were acquired within the amorphous area.

IV. EFFECTS OF HEAVY-ION IRRADIATION ON NORMAL-STATE RESISTIVITY AND CRITICAL TEMPERATURE

The effect of heavy-ion irradiation on the superconducting and normal-state transport properties of $YBa_2Cu_3O_{7-\delta}$ thin film were investigated as a function of the loss of superconducting volume fraction resulting from the amorphous tracks created by the ions. Because Cu^{18+} and Si^{13+} did not generate distinct linear defects during irradiation, measurements were made only on samples irradiated by gold and silver ions. Figure 15 shows the percentile change of the normal-state resistivity at 290 K and superconducting transition temperature versus the damaged area A, estimated from the size of the defects (the amorphous region). The zero-field critical temperature (T_c) before and after irradiation at fluence $\phi[T_c(\phi)]$ has been defined as the temperature at which the extrapolated normal-state resistivity above 90 K falls to half of its value. A universal linear increase in resistivity and suppression of the superconducting transition temperature is seen with the increase in the area of damage, irrespective of the ion type used. The magnitude of the degradation of the properties observed implies a substantial damage to the crystal lattice surrounding the amorphous defects. As shown in Fig. 15, irradiation with gold ions at a dose as low as 5.6×10^{10} ions/cm^2, which results in a defect separation equal to the flux line lattice spacing in an applied magnetic field of 1.3 T, causes nearly the same change in T_c and ρ(290 K), as that caused by Ag-ion irradiation at 2×10^{11} ions/cm^2. Thus, from the

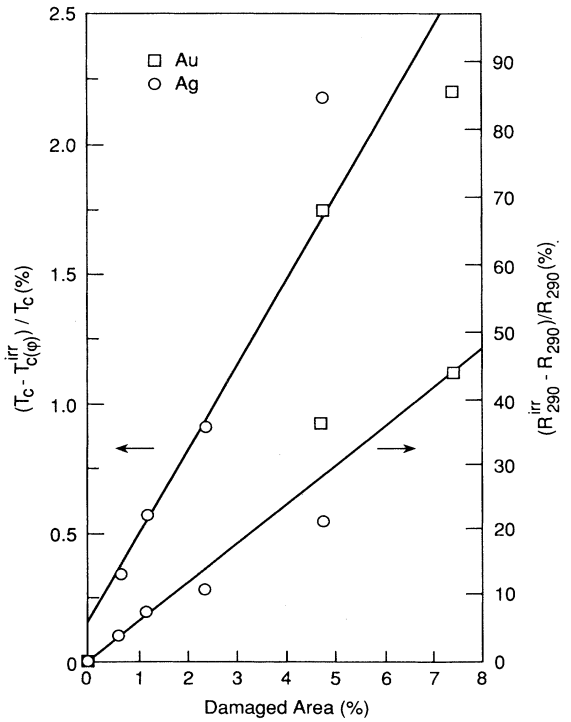

FIG. 15. Percentile changes in normal state resistivity (at 290 K) and transition temperature of $YBa_2Cu_3O_{7-\delta}$ thin films plotted as functions of the fractional areal damage.

viewpoint of optimizing the defect density to increase flux pinning and to limit the loss in superconducting volume, silver ions are much more suitable than the gold ions.

V. THERMAL SPIKE MODEL OF HEAVY-ION DAMAGE

A. Energy transfer and stopping power

An understanding of the formation and the structure of defects due to heavy-ion irradiation requires some knowledge of the mechanism by which the projectile deposits energy and how this energy is dissipated in the target crystal. In general, a charged particle moving through a solid medium can lose energy by three main processes. For ions with very high energy, the principal energy loss is due to interaction with the electrons of the crystal by Coulomb excitation or ionization. The ion also may lose energy by direct collision with nuclei of the crystal. The third process of energy loss is by radiation. Since the intensity of the emitted radiation is inversely proportional to the square of the mass of the incident particle, in the case of heavy ions, the energy loss due to radiation is negligible. Under the conditions of the present study, the energy loss caused by nuclear collisions, which can be estimated by the Rutherford scattering law, is two orders of magnitude less than the energy loss caused by electronic excitation due to the small scattering cross section of heavy ion. Thus, all of the energy deposition in the crystal as a heavy ion passes through essentially can be regarded as due to electronic excitations,[28] especially when the crystal is very thin compared with the estimated range (<200 nm of crystal thickness and >14 μm of the range in the present study). The rate of electronic energy loss, or the stopping power, depends on the characteristics of the incident ions, as well as on those of the target crystal. The dependence of the rate of the energy loss per unit length along the ion path (stopping power) due to electronic excitation upon these parameters is described approximately by the following expression due to Chadderton[29] (modified for a multicomponent target):

$$-\left.\frac{dE}{dx}\right|_{\text{electronic}} = \frac{2h^3}{\pi^2 m_e e^2}\left[\frac{2E}{M_1}\right]^{1/2} Z_1^{2/3}\sum_i n_i Z_i^{1/3} , \quad (2)$$

where Z_1 and Z_i are the atomic numbers of the incident and various target atoms i, respectively. n_i is the number of target atoms of type i per unit volume. E is the energy of the incident ion. M_1 and m_e are the mass of the incident ion and electron, respectively.

It may be seen from Eq. (2), that the stopping power rate depends on the kinetic energy and atomic number, as well as mass, of the incident ion. In Fig. 16, are plotted the measured diameters of the amorphous defects as a function of the stopping power ($-dE/dx$) for different samples. The values of ($-dE/dx$) of Au, Ag, Cu, and Si ions for $YBa_2Cu_3O_{7-\delta}$ and $Bi_2Sr_2Ca_2Cu_3O_x$ in this figure and in Tables I and II were calculated using the tables of Ziegler,[30] although the results are not too different from those using the less accurate Eq. (2). Although no conclusive observations can be drawn from these few data points, it appears that, for irradiation of a given material, the defect diameter versus stopping power follows an approximately parabolic relation. The threshold of the stopping power to form an amorphous defect (vertex of the parabolic curve) decreases with the decrease of oxygen concentration in the $YBa_2Cu_3O_{7-\delta}$ samples. For fully oxygenated $YBa_2Cu_3O_{7-\delta}$ ($\delta\approx 0.0$), the threshold of the stopping power is about 13 keV/nm. It is interesting to note that the curvature of the parabolic curve differs between $YBa_2Cu_3O_{7-\delta}$ and $Bi_2Sr_2Ca_2Cu_3O_x$. Although $Bi_2Sr_2Ca_2Cu_3O_x$ has smaller stopping powers for the various ions as compared to those of $YBa_2Cu_3O_{7-\delta}$, it yields much larger defects (by a factor of 1.4–2). For irradiation with Cu ions, amorphous-column defects were only occasionally observed in $YBa_2Cu_3O_{7-\delta}$, while frequently seen in $Bi_2Sr_2Ca_2Cu_3O_x$. This probably can be attributed to their difference in thermal conductivity as the thermal spike model discussed below suggests. For different materials, stopping power is clearly not the only criterion for evaluating the radiation damage.

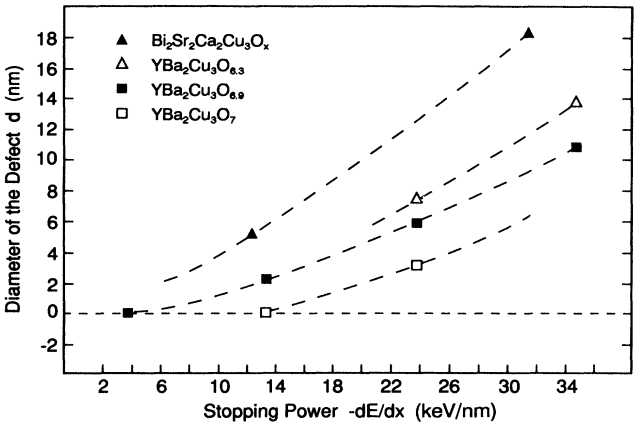

FIG. 16. Experimentally measured diameters of the columnar defects as a function of the stopping power ($-dE/dx$) for various samples of $YBa_2Cu_3O_{7-\delta}$ and $Bi_2Sr_2Ca_2Cu_3O_x$. The values of ($-dE/dx$) were calculated using the tables of Ziegler (Ref. 30).

A detailed investigation of the amorphization cross section created by heavy-ion irradiation of magnetic insulators was made by Studer and Toulemonde.[31] They found that the damage efficiency ε versus stopping power dE/dx curve follows as

$$\varepsilon=\varepsilon_{\max}\{1-\exp[k(dE/dx)^n]\} ,$$

where $\varepsilon_{\max}$ is the saturation efficiency, k varies with the material (decreasing when the material is less sensitive to the stopping power), and n is close to 4 for $Y_3Fe_2O_{12}$ and $BaFe_{12}O_{19}$.[32] Such a saturation law leads to the damage cross section being a linear function of (dE/dx) (Ref. 5) at the threshold and of (dE/dx) for the saturation regime, respectively. Our estimates of amorphous cross sections in Au- and Ag-irradiated $YBa_2Cu_3O_{7-\delta}$ shows that they are approximately proportional to the fifth

power of stopping power and suggests that the radiation damage we observed is in the threshold regime. This is consistent with Fig. 16.

B. A thermal spike model for the formation of the amorphous defects

Different models have been proposed to interpret the formation of heavy-ion irradiation-induced defects. The concept of "Coulomb explosions," i.e., the violent disruption of a local region of the lattice by unbalanced electrostatic forces during the period before electrical neutrality is restored to a region around the ion track in which charge separation is induced by the passage of the ions is popular.[33] However, developing a detailed model based on such concepts is quite difficult. Recently, however, a defense has been made of for the old notion of "thermal spikes," despite the use of continuum and linear heat-transfer approximations, in discussions of the damage process caused by swift ions, since "spikes do at least provide working models and a scenario which properly reflects the physics within the time scales involved."[33] Furthermore, the "spike" approximation has proved useful in rationalizing phase transformations and the formation of metastable phases caused by fission damage in metallic alloys.[34] Thus, in the following we use a thermal-spike model to discuss the formation of irradiation-induced defects.

First, the time needed for energy transfer from an incident ion to the excited electron gas is much less than the typical time scale of lattice vibration. Thus the energy loss from the incident ions can be regarded as instantly transferred to the gas of excited electrons. Then, the energy of electronic excitations is very quickly converted into thermal energy of the lattice in a very localized *region*. The rapidity with which the energy is transferred from the hot electrons to the lattice of ions depends on whether the material is metallic, semiconducting, or ionic, in increasing order of rapidity.[28,29]

The thermal energy then dissipates, so that thermal equilibrium can again be achieved. A theoretical model of this process will then consist of estimates of the energy deposited into the electron system by the heavy ion (as discussed in the previous section), the kinetics of the transfer of energy to heat the lattice ions, the transport of heat in the lattice, and the phase changes and defect formation which accompanies the rapid heating and quenching of the lattice. The dissipation of the energy by the diffusion of heat throughout the lattice will be approximately described by Fourier's linear law of heat conduction neglecting the effects of the latent heat of melting and freezing. The crudest approximation to the amorphized zone along the ion track is to assume that the entire region of the thermal spike where the temperature rises to or above the melting point becomes amorphous. (This will be an upper limit to the size in the context of a thermal-spike model.) Evidence that this approximation is incorrect and corrections to it will be discussed below.

To illustrate the main features of the thermal-spike model, we will first describe the simplest model, in which the energy of electronic excitations, assumed to be deposited in a line along the ion track, is instantaneously transferred to the lattice. (In the Appendix a more sophisticated model, which explicitly includes the transfer of energy from the electron excitations to the lattice, is described. The results of this two-component model can be quite well described by the simpler model with an effective thermal diffusivity.) An ion moving along the y axis parallel to the crystallographic b axis depositing an energy Q per unit of path length (equal to $-dE/dx$ from the previous section) will cause the temperature to rise above ambient temperature by an amount $\theta(x,z,t)$ where x and z are the distances from the ion track parallel to the a and c crystallographic axes, respectively, and t is the time after the passage of the ion. Assuming the heat transport is essentially isotropic in the a-b plane, standard solutions of the linear heat-transfer equations[35] yield:

$$\theta(x,z,t)=\frac{Q}{4\pi(D_{ab}D_c)^{1/2}t}\times\exp\left[-\left[\frac{x^2}{4D_{ab}}+\frac{z^2}{4D_c}\right]\frac{1}{t}\right], \tag{3}$$

where c is the heat capacity per unit volume and D_{ab} and D_c are the thermal diffusivities for directions in the a-b plane and along the c axis, respectively. At a given location the temperature will rise rapidly to a maximum value and then cool more slowly back to the ambient temperature. A given isotherm of θ will be an ellipse which expands rapidly from zero to a maximum size and then shrinks more slowly back to zero, sort of a "big bang" followed by a "big crunch" on a microscopic rather than a cosmological scale. Equation (3) can also be used for ion trajectories along the c axis by replacing D_c by D_{ab}. In that case, the θ isotherms become expanding and contracting circles, rather than ellipses. The time dependence of the diameter $d_m(t)$ of the circular isotherm corresponding to the melting point of $YBa_2Cu_3O_6$ is shown in Fig. 17. (The curves for $YBa_2Cu_3O_7$ are cal-

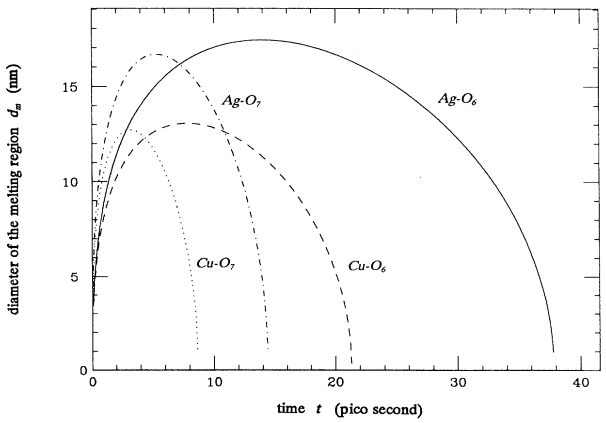

FIG. 17. The calculated time dependence of the diameter $d_m(t)$ of the molten zone after the passage of a heavy ion for $YBa_2Cu_3O_6$ irradiated by Ag (solid line) and Cu (dashed line) and for $YBa_2Cu_3O_7$ irradiated by Ag (dot dashed line) and Cu (dotted line). The calculations were made as described in the Appendix.

culated using the more elaborate model described in the Appendix.) It is readily shown from Eq. (3) that when the ion tracks are parallel to the c axis the diameter $d_{\max}$ of the circular region in which the temperature has reached or exceeded the melting point is

$$d_{\max}=(4Q/\pi eC\theta_{\mathrm{mp}})^{1/2}\ , \tag{4}$$

where e is the base of natural logarithms and θ_{mp} is the difference between the melting point and the ambient temperature when the ion travels parallel to the a or b axis. The major and minor diameters of the elliptical area in which the temperature reaches or exceeds the melting point are

$$d_{ab}=d_{\max}(D_{ab}/D_c)^{1/4}\ , \tag{5}$$

$$d_c=d_{\max}(D_c/D_{ab})^{1/4}\ . \tag{6}$$

These results, Eqs. (4)–(6), are in qualitative agreement with the experimental data. The calculated values of $d_{\max}$, collected in Table II for $YBa_2Cu_3O_{7-\delta}$, are of the same order of magnitude as the diameters of the amorphous defects but exceed the experimentally measured values by about 10 nm. The simplest explanation, aside from the obvious one that the model is simply too crude, is that the molten region does not all become amorphous, but some epitaxial regrowth occurs during the cooling down period and the diameter of the amorphous region is thus smaller than that of the original molten zone, and in the case of Si and sometimes Cu, the crystalline regrowth can be essentially complete, albeit with some lattice defects remaining. This is consistent with the observation of stacking faults created in association with the columnar defects and extending to a size 3–5 times that of the amorphous region, as discussed in Sec. III F above.

The observed ellipticity of columnar defects created by ions traveling along the a or b axis (see Figs. 7–9) is qualitatively consistent with predictions of Eqs. (5) and (6), but the quantitative values of d_{ab}/d_c also suggest the existence of partial epitaxial regrowth of the molten ion track. The model predicts that the largest diameter of the elliptically shaped cross section of an a-axis track will be in the direction of the largest component of thermal diffusivity, i.e., the b direction, as was observed. For a gold ion of 300-MeV energy, we estimate a value of about 20 nm for an upper limit to the diameter of a c-axis track for $YBa_2Cu_3O_{7-\delta}$. The observed diameter for a c-axis track in $YBa_2Cu_3O_{6.3}$ is about 11 nm, while the geometric mean of the two diameters of an elliptically cross-sectioned a-axis track was observed to be about 16 nm. [Note that Eqs. (4)–(6) predict that in the absence of epitaxial regrowth the diameter of the c-axis track should equal the geometric mean of the two diameters for an a-axis track, provided there is no crystallographic orientation dependence of the energy deposition rate for an ion of a given energy.] The ratio of the diameters of the elliptical cross section is predicted to be $(D_{ab}/D_c)^{1/2}$. The ratio could be as large as about 3–5 for $YBa_2Cu_3O_7$ (Refs. 36–39) (a slightly reduced value is expected for $YBa_2Cu_3O_{6.3}$) compared to the observed value of about 1.5. While the quantitative discrepancies between the theoretical predictions and the observations may simply reflect the simplicity of the model, it is possible that they also result from the neglect of epitaxial regrowth of a portion of the molten region. This effect could account for the smaller size of the observed track cross section than predicted and for the smaller observed eccentricity of the elliptical cross section, since for cuprates the crystal's growth rate parallel to the a-b planes has been widely observed to exceed that perpendicular to it, hence, making the remaining amorphous region less eccentric than the original molten region.

As the discussion above indicates, several pieces of experimental evidence suggest that the simplest model, which assumes that the entire region for which the temperature exceeds the melting point becomes amorphized, must be modified to account for partial epitaxial regrowth. Several physical processes should be considered, among them: whether or not the cooling rate is sufficiently fast to quench in the disorder of the liquid phase; at what point the velocity of the solid-liquid interface, which retreats at an accelerating rate (i.e., the "big crunch" portion of the curves in Fig. 17), becomes too large to permit epitaxial regrowth; and others. A detailed investigation of the role of these processes is beyond the scope of this paper. Another factor for multicomponent materials such as the cuprates which often melt incongruently,[40] is the length of time which a given region stays at a temperature above the melting point,

TABLE II. Calculated energy loss and calculated and measured diameter d of the damaged area for $YBa_2Cu_3O_{7-\delta}$ by various incident ions. $d_{\max}$ denotes the calculated diameter of the molten region; $t_{\max}$ denotes the time required for the molten zone to reach its maximum extent.

Ion	Au	Ag	Cu	Si
Energy loss (keV/nm)	34.8	23.8	13.4	3.8
d for O_6 cal. (nm), $\Delta t_c=20$ ps	21.0	15.0	5.0	0
$d_{\max}$ for O_6 cal. (nm)	22.0	17.5	13.0	7.0
$t_{\max}$ for O_6 cal. (ps)	22	16	8	2
d for $O_{6.3}$ meas. (nm)	13.5	7.0		
d for O_7 cal. (nm), $\Delta t_c=14$ ps	14.0	4.0	0	0
$d_{\max}$ for O_7 cal. (nm)	20.0	16.8	12.8	6.8
$t_{\max}$ for O_7 cal. (ps)	7.5	5.5	3.2	1.1
d for $O_{6.9}$ meas. (nm)	10.5	5.5	2.2	0
d for O_7 meas. (nm)		3.0	<1.2	0

thus permitting rearrangements of the short-range order, clustering and segregation, etc., which hinder the subsequent epitaxial regrowth and favor the retention of an amorphous phase. For the purposes of this discussion we introduce a simple heuristic device which accounts in some fashion these effects: the concept of a critical length of time Δt_c which a given region of material must remain above the melting point in order to be retained in an amorphous state. We shall see that this heuristic modification of the simple model yields semiquantitative agreement with the observed dependence of the diameter of the amorphous columns and with the observation that the threshold energy deposition rate for amorphous defect formation increases with increasing oxygenation (and hence increasing thermal diffusivity with increasing mobile carrier density) in $YBa_2Cu_3O_{7-\delta}$ (as seen in Fig. 16).

The diameter d of the column of material which has remained above the melting point for a period Δt_c is given by the value of $d_m(t)$ for which the breadth of a heating-cooling curve, such as those shown in Fig. 17, is Δt_c. The equation for $d_m(t)$ which follows from the modification of Eq. (3) for an ion moving parallel to the c axis is given by Eq. (A12) in the Appendix. Numerical calculations show that an approximation good to within a few percent for the variation of d with Δt_c is

$$d \cong d_{\max}\left[1-\left[\frac{16D_{ab}}{ed_{\max}^2}\Delta t_c\right]^2\right]^{1/2}, \tag{7}$$

where $d_{\max}$ is the maximum of the heating-cooling curve, given by Eq. (4), and e is the base of natural logarithms. Note that this equation implies the existence of a threshold value of $d_{\max}$, and by Eq. (4) a threshold value of $Q \equiv -dE/dx$, for a given value of Δt_c. For a nonzero value of the radius d of the column of amorphous material, the energy deposition rate Q must obey

$$Q > Q_{\text{threshold}} \equiv 4\pi D_{ab} C \theta_{\text{mp}} \Delta t_c \ . \tag{8}$$

Note that the threshold rises with increasing thermal diffusivity, consistent with the data for $YBa_2Cu_3O_{7-\delta}$ shown in Fig. 16. The experimental data show that $Q_{\text{threshold}}$ ranges from about 4 to 13 keV/nm. Equation (8), with the values of D_{ab} and C listed in the Appendix, thus yields Δt_c in the range 10–40 ps, which is consistent with the ps time scale of atomic jumps in liquids. Values of d for various ions, calculated from the curves of Fig. 17 or, equivalently, with Eq. (7), with Δt_c of 14 and 20 ps for $YBa_2Cu_3O_7$ and $YBa_2Cu_3O_6$, respectively, are listed in Table II. The calculated values are in reasonable agreement with the experimentally observed values. Thus, we see that the anisotropic thermal-spike model, together with the notion of a critical time interval in the liquid state needed to retain amorphicity and prevent epitaxial regrowth, is capable of a semiquantitative description of a number of aspects of heavy-ion damage in cuprate superconductors.

VI. SUMMARY

We have conducted a comprehensive study of structure and properties of high-T_c superconductors irradiated with ions of Si, Cu, Ag, and Au with an energy ranging from 182 to 300 MeV. Au^{24+} and Ag^{21+} radiations lead to the formation of columnar defects in the materials. These columns consist of amorphized material within the envelope of a region of lattice defects and a displacement/strain field which propagates into the crystal lattice. No distinct radiation damage was observed by TEM in samples irradiated with Si^{13+} ions. For Cu^{18+}, amorphous defects were frequently observed in $Bi_2Sr_2Ca_2Cu_3O_x$, but not in $YBa_2Cu_3O_{7-\delta}$. For fully oxygenated $YBa_2Cu_3O_{7-\delta}$ ($\delta \approx 0.0$), the threshold of the stopping power to form the amorphous column was found to be 13 keV/nm. We also found that the degree of the radiation damage by the heavy ions depends on the rate of the energy loss ($-dE/dx$) of the ion, the relationship of crystallographic orientations to the incident ion, the stoichiometry of the sample, the perfection of the crystal, and the thermal conductivity of the target as well. A simple anisotropic thermal-spike model based on the idea of ion-induced localized melting and partial epitaxial regrowth was proposed to describe the formation of the amorphous tracks and which agrees at least semiquantitatively with many of the observed features. Measurements of the superconducting transition temperature, and the normal-state resistivity of $YBa_2Cu_3O_{7-\delta}$ films irradiated with Au^{24+} and Ag^{21+} ions reveal a universal linear scaling between the fractional areal damage versus the superconducting transition temperature and the normal-state resistivity.

ACKNOWLEDGMENTS

The authors would like to thank Charles W. Carlson, V. Zajic, and the control room staff at Tandem Van de Graaff for their cooperation during the irradiation experiments. They also thank A. R. Moodenbaugh for preparation of $YBa_2Cu_3O_{7-\delta}$ and H. Ikeda and R. Yoshizaki for $Bi_2Sr_2Ca_2Cu_3O_x$ ($x \approx 10$) specimens. This research was supported by the U.S. Department of Energy, Division of Materials Sciences, Office of Basic Energy Sciences under Contract No. DE-AC02-76CH00016. The use of Philips 400T FEG microscope was partially sponsored by the Division of Materials Sciences, U.S. Department of Energy, under Contract No. DE-AC05-84OR21400 with Martin Marietta Energy Systems, Inc., and through the SHaRE Program under Contract No. DE-AC05-76OR00033 with Oak Ridge Associated Universities. The use of the H-9000 and HF-2000 microscopes in the Department of Materials Science and Engineering at Northwestern University is also gratefully acknowledged.

APPENDIX: A THERMAL-SPIKE MODEL WHICH EXPLICITLY INCLUDES AN ELECTRON GAS COOLED TO A LATTICE OF IONS

1. Energy transfer to the lattice

As discussed in Sec. V A, the energy initially transferred to the sample from the fast moving heavy ion

is predominantly in the excited electrons. Here we discuss how the energy transfers from the gas of excited electrons to the lattice to create defects. Because of the short time required to excite electrons, we can assume that all the energy has been transferred to the electron gas at time $t=0$. It is also reasonable to assume at the electron gas is in equilibrium at any time. A simple coupled thermal diffusion model which evaluates the energy transfer from electron gas to the atoms was first described by Chadderton,[28,29] and we make use of this model here.

Assume an electron gas with a temperature θ_1 above the ambient temperature which is homogeneously mixed with a gas of heavy atoms with a temperature θ_2 above the ambient. The heat transport may be represented by the pair of linear differential equations:

$$\kappa_1\frac{\partial^2\theta_1}{\partial x^2}=C_1\frac{\partial\theta_1}{\partial t}+b(\theta_1-\theta_2)\ , \tag{A1}$$

$$\kappa_2\frac{\partial^2\theta_2}{\partial x^2}=C_2\frac{\partial\theta_2}{\partial t}-b(\theta_1-\theta_2)\ , \tag{A2}$$

where κ_1 and κ_2 are the thermal conductivities of electrons and atoms, respectively, C_1 and C_2 are the heat capacities per unit volume, and b is a coupling coefficient of heat transfer between electron and atoms. As in the case of a homogeneous mixture of perfect gases $C_1\cong C_2\equiv C$, so that we may let

$$\kappa_1/C=D_1\ , \tag{A3}$$

$$\kappa_2/C=D_2\ , \tag{A4}$$

$$b/C=\mu\ . \tag{A5}$$

Solutions to Eqs. (A1) and (A2) may be derived by substitutions of the form

$$\theta_1=\alpha_1\exp(ikx+\phi t)\ , \tag{A6}$$

$$\theta_2=\alpha_2\exp(ikx+\phi t) \tag{A7}$$

into Eqs. (A1) and (A2). We then find that

$$\phi=-\mu-\frac{(D_1+D_2)}{2}k^2+\left[\left[\frac{D_1-D_2}{2}\right]^2+\mu^2\right]^{1/2}\ . \tag{A8}$$

For an instantaneous line source produced initially entirely in the electron gas, the solution for the lattice temperature θ_2 becomes

$$\theta_2=\frac{Q}{2\pi C}\exp(-\mu t)\int_0^\infty\exp[-(D_1+D_2)k^2t/2]\times\frac{\sinh(\mu t\sqrt{1+\delta^2})}{\sqrt{1+\delta^2}}J_0(kr)k\,dk\ , \tag{A9}$$

where

$$\delta=\frac{(D_1-D_2)}{2\mu}k^2\ .$$

We will compare the lattice temperature (θ_2) with the melting temperature of the YBCO compounds ($\theta_{\rm mp}$ is approximately 1000 K). The melting region has a diameter of $d_m(t)$ where

$$\theta_2(r=d_m/2,t)=\theta_{\rm mp}\ . \tag{A10}$$

For the purposes of these calculations, we utilize the following values for the parameters: the electron-lattice coupling constant μ is assumed, following Chadderton[28,29] to be 10 ps^{-1}. The specific-heat capacity per unit volume C is taken to be the Dulong-Petit limit, 1.84×10^{-5} eV $Å^{-2}K^{-1}$; the experimentally observed[35] thermal conductivity for YBCO at high temperatures is observed to be about 4 $JM^{-1}s^{-1}K=0.0025$ eV $Å^{-1}ps^{-1}K^{-1}$ and we use this value for the lattice thermal conductivity κ_2 which corresponds to a lattice thermal diffusivity $D_2=\kappa_2/C$ of 136 $Å^2ps^{-1}$. The value of the electron thermal diffusivity depends upon the oxygenation of the compounds, as discussed below.

2. $YBa_2Cu_3O_6$: The semiconductor

For a semiconductor, the thermal diffusivity of the electron gas is about the same order of magnitude as that of the lattice, i.e., $D_1=D_2$. We therefore have, from Eq. (A9),

$$\theta_2=\frac{Q}{2C}\frac{1}{4\pi D_2t}\exp\left[\frac{-r^2}{4D_2t}\right][1-\exp(-2\mu t)]\ . \tag{A11}$$

When nearly all the energy is transferred to the lattice, the second term can be ignored. The diameter d_m of the molten zone then becomes

$$d_m(t)=4\left[D_2t\ln\left[\frac{Q}{8\pi CD_2t\theta_{\rm mp}}\right]\right]^{1/2}\ . \tag{A12}$$

The calculated time dependence of the diameter of the molten region d_m for Ag and Cu ions irradiating $YBa_2Cu_3O_6$ is shown in Fig. 17. The values of the maximum diameter $d_{\rm max}$ of the molten region and the time $t_{\rm max}$ required to achieve the maximum size are listed in Table II.

3. $YBa_2Cu_3O_7$: The metal

For a metal, $D_1\gg D_2$, and we have

$$\theta_2=\frac{Q}{2\pi C}\exp(-\mu t)\int_0^\infty\exp\left[-\frac{D_1k^2t}{2}\right]\frac{\sin(\mu t\sqrt{1+D_1^2k^4/4})}{\sqrt{1+D_1^2k^4/4}}J_0(kr)k\,dk\ . \tag{A13}$$

The numerical results for $YBa_2Cu_3O_7$ listed in Table II and shown in Fig. 17, were calculated using $D_1 = 5D_2$. We also did calculations for the case of $D_1 = 10D_2$ and no significant change is found. These results show that even though the energy loss and the assumed value of the electron-lattice coupling in $YBa_2Cu_3O_7$ are almost the same as in $YBa_2Cu_3O_6$, the higher diffusivity of electrons in the metallic $YBa_2Cu_3O_7$ causes the time required for the temperature at a given position to reach the melting point to be much shorter than in the $YBa_2Cu_3O_6$ case. In fact, the resulting curves of the time-dependent radius of the molten zone $R_m(t)$, e.g., Fig. 17, resulting from Eq. (A13) can be described well by Eq. (A12) with an effective thermal diffusivity D_{eff} which depends slightly on the energy of the incident ion: the ratio of D_2^{eff} to D_2 is found to be 2.9, 2.9, 2.5, and 2.0, respectively, for Au, Ag, Cu, and Si ions with the energies listed in Table I.

[1]For a review see A. R. Sweedler, C. L. Snead, Jr., and D. E. Cox, in *Treatise on Materials Science and Technology,* Vol. 14, edited by T. Luhman and D. Dew-Hughes (Academic, New York, 1979), pp. 349–426.

[2]H. W. Weber and G. W. Crabtree, in *Studies of High Temperature Superconductors,* edited by A. V. Narlikar (Nova Scientific, New York, 1992), Vol. 9, pp. 37–39.

[3]L. Civale, A. D. Marwick, M. W. McElfresh, T. K. Worthington, A. P. Malozemoff, F. Holtzberg, J. R. Thompson, and M. A. Kirk, Phys. Rev. Lett. **65**, 1164 (1990).

[4]R. B. van Dover, E. M. Gregory, A. E. White, L. F. Schneemeyer, R. J. Felder, and J. V. Waszczak, Appl. Phys. Lett. **56**, 2681 (1990).

[5]W. Schindler, B. Raos, G. Saemann-Ischenko, L. Schultz, and H. Gerstenberg, Physica C **169**, 117 (1990).

[6]D. Bourgault, D. Groult, S. Bouffard, J. Provost, F. Studer, N. Nguyen, B. Raveau, and M. Toulemonde, Phys. Rev. B **39**, 6549 (1989).

[7]B. Hensel, B. Roas, S. Henke, R. Hopfengrtner, M. Lippert, J. Ströbel, M. Vildic, and G. Saemann-Ischenko, Phys. Rev. B **42**, 4135 (1990).

[8]L. Civale, A. D. Marwick, T. K. Worthington, M. A. Kirk, J. R. Thompson, L. Krusin-Elbaum, Y. Sun, J. R. Clem, and F. Holtzberg, Phys. Rev. Lett. **67**, 648 (1991).

[9]M. Konczykowski, F. Rullier-Albenque, E. R. Yacoby, A. Shanlov, Y. Yeshurun, and P. Lejay, Phys. Rev. B **44**, 7167 (1991).

[10]W. Gerhauser, G. Ries, H. W. Neumuller, W. Schmidt, O. Eibl, G. Saemann-Ischenko, and S. Klaumunzer, Phys. Rev. Lett. **68**, 879 (1992).

[11]V. Hardy, D. Grout, M. Hervieu, J. Provost, and B. Ravean, Nucl. Instrum. Methods B **54**, 472 (1991); Physica C **191**, 255 (1992); V. Hardy, D. Grout, J. Provost, and B. Ravean, *ibid.* **190**, 289 (1992); V. Hardy, J. Provost, D. Grout, M. Herrien, B. Ravean, S. Durcok, E. Pollert, J. C. Frison, J. P. Chaminade, and M. Pouchard, *ibid.* **191**, 85 (1992).

[12]R. C. Budhani, Y. Zhu, and M. Suenaga, Appl. Phys. Lett. **61**, 985 (1992); R. C. Budhani and M. Suenaga, Solid State Commun. **84**, 8312 (1992).

[13]R. C. Budhani, M. Suenaga, and S. H. Liou, Phys. Rev. Lett. **69**, 3816 (1992).

[14]H. Ikeda, R. Yoshizaki, and K. Yoshikawa, Cryogenic Eng. **25**, 99 (1990).

[15]Y. Zhu, R. C. Budhani, Z. X. Cai, D. O. Welch, M. Suenaga, R. Yoshizaki, and H. Ikeda, Philos. Mag. Lett. **67**, 125 (1993).

[16]Y. Zhu, R. L. Sabatini, Y. L. Wang, and M. Suenaga, J. Appl. Phys. **73**, 3407 (1993).

[17]Y. Zhu, Z. L. Wang, and M. Suenaga, Philos. Mag. A **67**, 11 (1993).

[18]H. P. Degischer, Philos. Mag. **26**, 1137 (1972).

[19]Y. Zhu, Z.-X. Cai, and D. O. Welch (unpublished).

[20]M. F. Ashby and L. M. Brown, Philos. Mag. **8**, 1083 (1963).

[21]A. E. H. Love, *The Mathematical Theory of Elasticity* (Dover, New York, 1944), Sections 99 and 100.

[22]H. W. Weber, Super Sci. Technol. **5**, S19 (1992).

[23]M. J. Kramer, Q. Qian, D. Finnemore, and C. L. Snead, Physica C **203**, 83 (1992).

[24]Y. Zhu, H. Zhang, M. Suenaga, and D. O. Welch, Philos. Mag. (to be published).

[25]N. Nücker, J. Fink, T. C. Fuggle, P. J. Durham, and W. M. Temmerman, Phys. Rev. B **37**, 5158 (1988).

[26]T. Takahashi, H. Matsuyama, T. Watanabe, H. Katayama-Yoshida, S. Sato, N. Kosugi, A. Yagishita, S. Shamoto, and M. Sato, in *Proceedings of the 3rd International Symposium on Superconductors,* edited by K. Kajimura and H. Hayakawa (Springer-Verlag, Berlin, 1990), p. 75.

[27]Z. X. Cai (unpublished).

[28]L. T. Chadderton and I. M. Torrens, *Fission Damage in Crystals* (Methuen, London, 1969), Chaps. 2 and 12.

[29]L. T. Chadderton, Nucl. Tracks Radiat. Meas., Int. J. Radiat. Appl. Instrum. Part D **15**, 11 (1988).

[30]J. F. Ziegler, *Handbook of Stopping Cross-Sections For Energetic Ions in All Elements* (Pergamon, New York, 1980).

[31]F. Studer and M. Toulemonde, Nucl. Instrum. Methods B **65**, 560 (1992).

[32]A. Meftah, N. Merrien, N. Nguyen, F. Studer, H. Pascard, and M. Toulemonde, Nucl. Instrum. Methods B **59/60**, 605 (1991).

[33]B. E. Fischer and R. Spohr, Rev. Mod. Phys. **55**, 970 (1983).

[34]G. J. Dienes and G. H. Vineyard, *Radiation Effects in Solids* (Interscience, New York, 1957), Sec. 3.4.

[35]H. S. Cardslaw and J. C. Jaeger, *Conduction of Heat in Solids,* 2nd Ed. (Oxford University Press, New York, 1959).

[36]D. M. Ginsberg, *Physical Properties of High Temperature Superconductors I* (World Scientific, Singapore, 1989).

[37]S. J. Hagar, Z. Z. Wang, and N. P. Ong, Phys. Rev. B **40**, 9389 (1989).

[38]M. Seva, S. Shamoto, M. Sato, I. Watanabe, S. Nakashima, and K. Kumagi, Solid State Commun. **74**, 951 (1990).

[39]S. C. Cao, S.-C. Zhang, D.-M. Zhang, H. M. Duan, and M. Herman, Phys. Rev. B **44**, 12 571 (1991).

[40]T. Aselage and K. Keefer, J. Mater. Res. **3**, 1279 (1988).

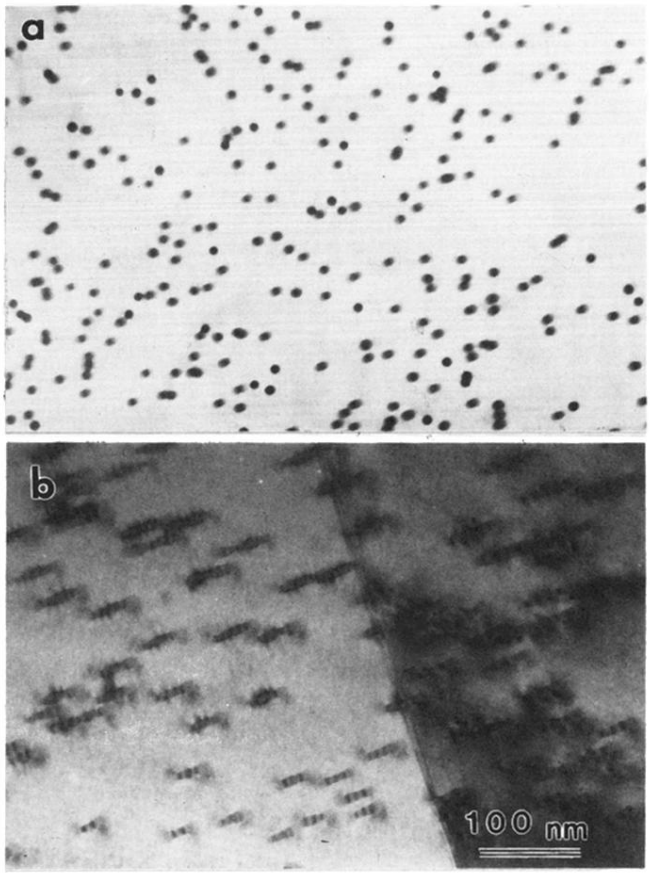

FIG. 1. Typical morphology of the Au^{24+}-radiation-induced defects viewed (a) along the ion track, (b) about 18° away from the ion track.

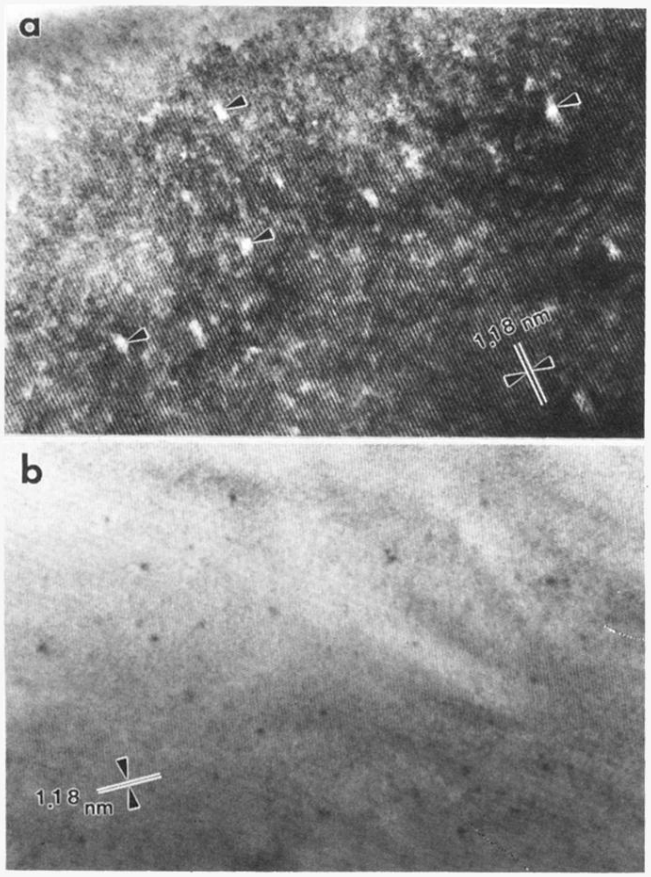

FIG. 11. Lattice image of [001] projection observed in $YBa_2Cu_3O_{7-\delta}$. (a) Cu ion irradiated without ozone treatment. The arrows denote defects in which the amorphous column extends completely through the sample. Other defects can be seen which show a superposition of amorphous and crystalline regions along the ion track. (b) Cu ion irradiated after ozone treatment.

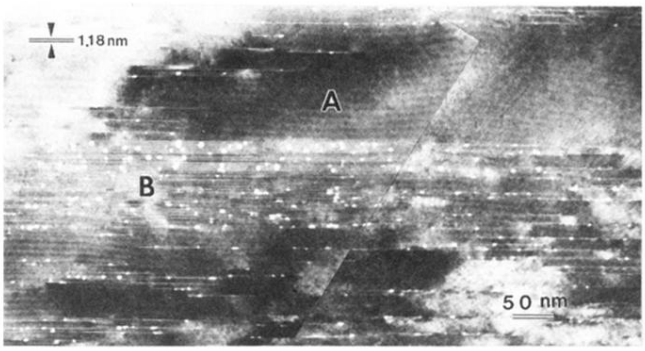

FIG. 12. (100) lattice image of an ozone-treated sample of $YBa_2Cu_3O_{7-\delta}$ ($\delta \cong 0$) irradiated with Cu ions. Note, the columnar defects were only observed at the location of the preexisting stacking faults.

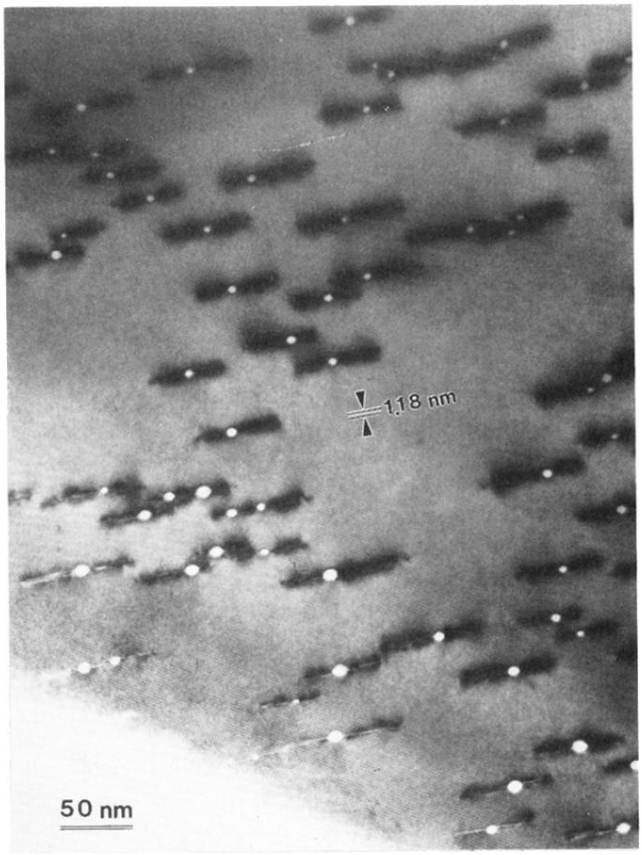

FIG. 13. (100) lattice image of $YBa_2Cu_3O_{7-\delta}$ ($\delta < 0.1$) irradiated with Ag ions showing stacking faults, viewed edge on, created by the radiation damage. The stacking faults are seen as dark wide lines in thick region and white narrow lines in thin region.

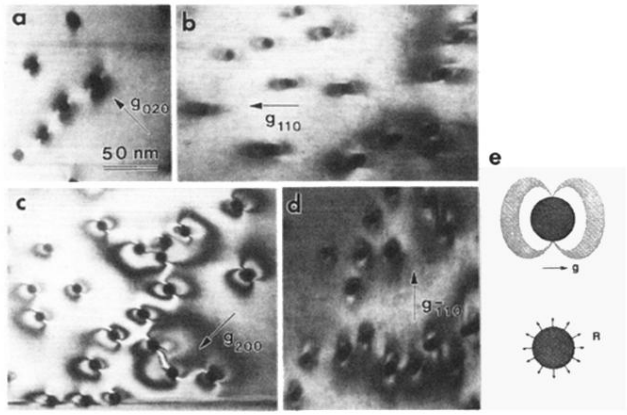

FIG. 2. Strain contrast surrounding the columnar defects imaged using diffraction vectors (a) $\mathbf{g}=020$, (b) $\mathbf{g}=110$, (c) $\mathbf{g}=200$, and (d) $\mathbf{g}=-110$. Note the contrast disappears in the direction perpendicular to the $\mathbf{g}$. (e) Sketches of the strain contrast and the displacement field due to the columnar defect.

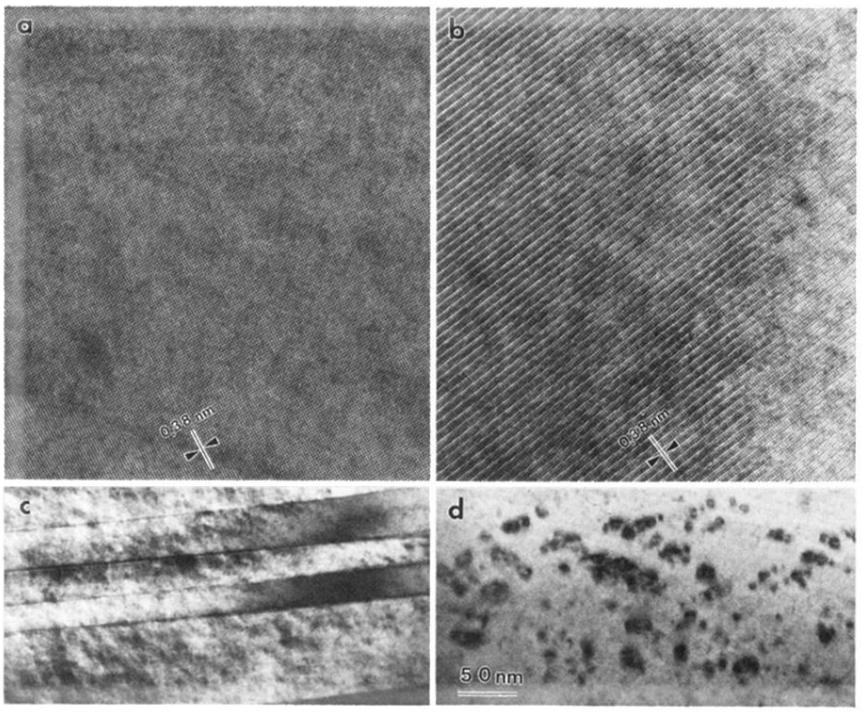

FIG. 3. TEM micrographs on Si-irradiated samples: (a) lattice images of a [001] projection, (b) [100] projection, (c) low-magnification two-beam image, and (d) dislocation loops.

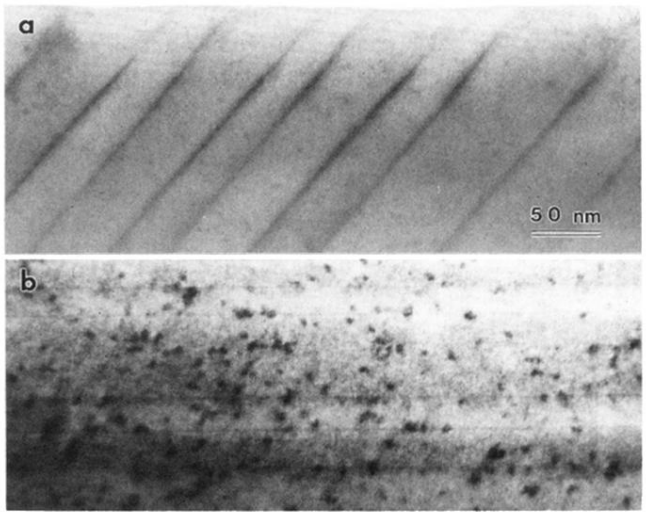

FIG. 4. The degree of the radiation damage seen in TEM caused by Cu ions varies with location in the specimen. (a) and (b) are views with the electron beam near the [001] axis of two different regions of a sample of $YBa_2Cu_3O_{7-\delta}$ $(0.1 < \delta < 0)$. Note, the defects do not exhibit the same type of strain contrast shown by "regular" columns, as in Fig. 2. In some areas, even the weak strain contrast seen in (b) cannot be observed. [The approximately linear features seen in (a) and (b) are twin boundaries.]

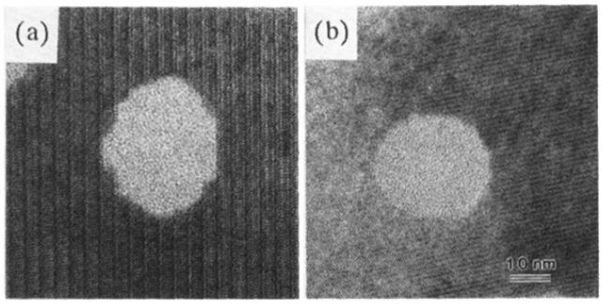

FIG. 7. High-resolution images of Au^{24+} irradiation-induced defects in bulk $Bi_2Sr_2Ca_2Cu_3O_x$ recorded in (a) [100], and (b) [001] projections, respectively.

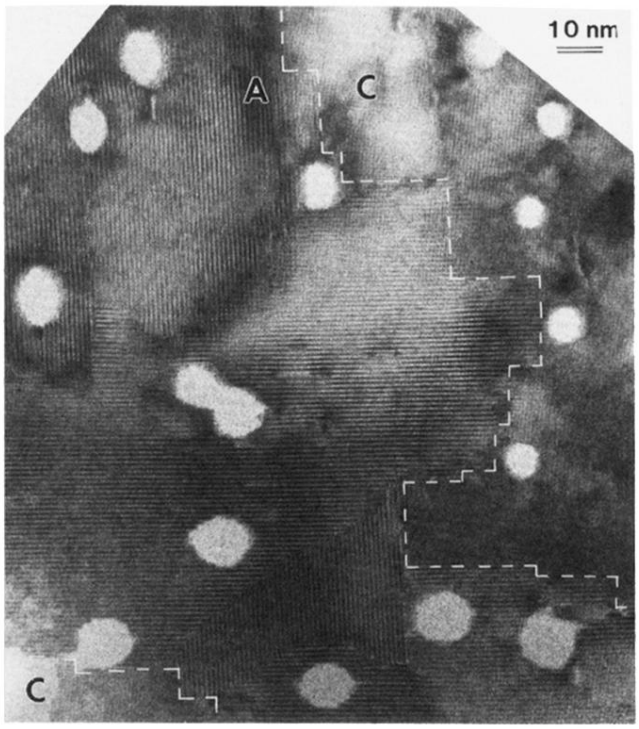

FIG. 8. High-resolution image of Au^{24+}-irradiated $YBa_2Cu_3O_7$ thin film. The defects appear elliptical in shape when the incident ion is parallel to the [100] (or [010]) direction, but smaller and circular in shape when parallel to the [001] direction. The areas denoted *A* and *C* have the *a* (or *b*) and *c* axes parallel to the film normal, respectively.

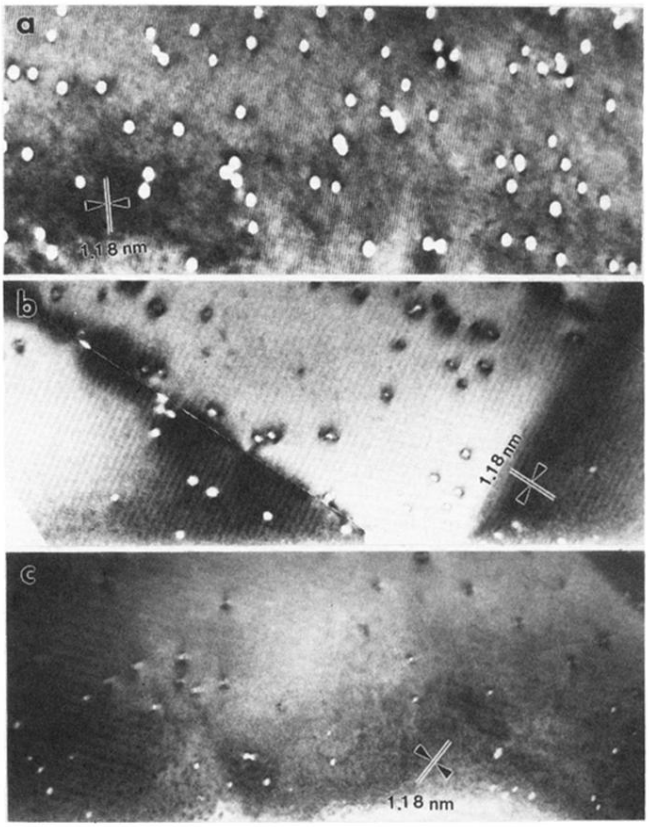

FIG. 9. Columnar defects induced by Ag-ion radiation viewed along [100] direction. (a) $YBa_2Cu_3O_{6.3}$, (b) $YBa_2Cu_3O_{7-\delta}$ ($0 < \delta < 0.1$), and (c) ozone-treated $YBa_2Cu_3O_{7-\delta}$ ($\delta \approx 0$).